Carrier Plasmon-Polar Phonon Coupling at Semiconductor Surfaces

Sci. Rep. RITU A41 (1996) pp. 119-131
No. 2, January 1996

Carrier Plasmon-Polar Phonon Coupling at Semiconductor Surfaces

Takeshi Inaoka

Department of Materials Science and Technology, Faculty of Engineering, Iwate University, 4-3-5 Ueda, Morioka, Iwate 020, Japan
(Received November 14, 1995)

We investigate the carrier plasmon-polar phonon coupling at semiconductor surfaces by taking account of the dielectric response of a semi-infinite carrier-electron gas and the polar-phonon polarization. The dynamical response of carriers is treated with the random-phase approximation, and the phonon polarization is described by the Lorentzian oscillator model. The coupling character of each coupled surface mode can be clarified by decomposing the induced charge-density distribution into a carrier component due to carrier density fluctuation, a phonon component originating from longitudinal polar-phonon polarization, and two on-surface components arising from termination of the phonon and the background polarization at the surface. The spatial structure of each surface mode can be visualized in the contour map showing the induced charge-density distribution and in the electric-field profile. We examine the coupling character and the spatial structure of each coupled surface mode, the evolution of the character and the structure of each mode with change of carrier concentration, and the origin of three coupled surface modes.

KEYWORDS: carrier plasmon, polar phonon, semiconductor surface, coupling character, spatial structure

1. Introduction

In doped semiconductors, energy values of carrier plasmons can be varied by controlling the doping level, and in polar semiconductors, carrier plasmons are coupled with polar phonons, when energy values of the former become comparable to those of the latter. Coupled plasmon-polar phonon modes in the bulk were observed by Raman scattering measurements, and their spectra were quantitatively analyzed by means of a theoretical framework which combines the random-phase approximation (RPA) scheme with the Lorentzian oscillator model.[1-4] Figure 1 exhibits the energy dispersion of coupled bulk modes in n-doped degenerate InSb with carrier concentration $n=1.463\times10^{17}$ cm^{-3} (Fermi wavenumber $k_F=1.630\times10^{6}$ cm^{-1}). The single-particle excitation (SPE) continuum extends on the right side of the dotted curve, and the energy-loss intensity decays away on the broken curves. There exist three dispersion branches, two of which lie in the smaller-wavenumber region outside the SPE continuum, and the third of which extends in the larger-wavenumber region. The former two branches arise from carrier plasmon-polar phonon coupling, while the latter branch is the longitudinal optical phonon which suffers the screening effect due to carriers. The induced charge density $\delta\rho$ can be decomposed into a carrier component $\delta\rho_{EL}$ due to carrier density fluctuation and a phonon component $\delta\rho_{PH}$ originating from longitudinal polar-phonon polarization. The mode structure can be clarified by examining the phase relation and the amplitude ratio of $\delta\rho_{EL}$ and $\delta\rho_{PH}$.[5] Each of these three branches has its own characteristic mode structure. The above decomposing scheme has shown how the mode structure varies with change of carrier concentration through the strong-coupling concentration regime.[5]

As for semiconductor heterostructures, the electron-optical phonon coupling in heterostructures has been investigated by using orthonormal phonon eigenmodes calculated in the dielectric continuum model.[6] This investigation has derived the Hamiltonian which describes an effective electron-electron interaction mediated by virtual exchange of phonons.

In the presence of the surface, the carrier density decreases and vanishes at the surface. In the case of carrier systems in semiconductors, the characteristic length to describe the variation of the carrier density near the surface is much longer than that to describe the penetration of electronic states into the vacuum. Therefore, it is a good approximation to assume that carriers are restrained in the materiel by an infinite barrier at the surface. In addition, there occur induced charges right on the surface owing to

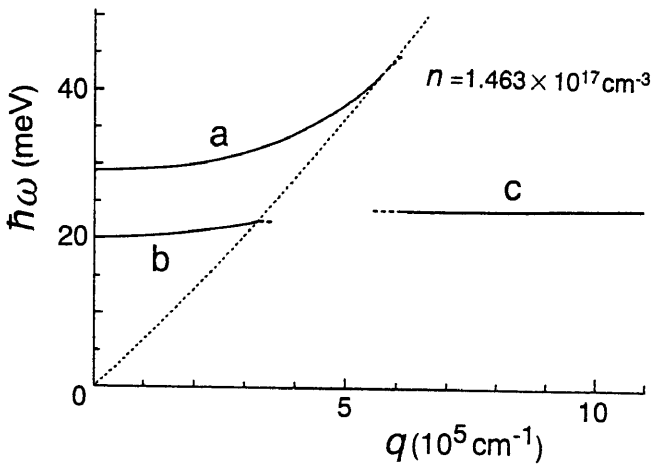

Figure 1. Energy dispersion of coupled bulk modes in n-type degenerate InSb with $n=1.463\times10^{17}$ cm^{-3}.

termination of the polar-phonon and background polarization at the surface.

Coupled surface modes of doped polar semiconductors such as n-type GaAs ,[7-11] InSb[12,13] and InAs[14,15] have been observed by high-resolution electron energy loss spectroscopy (HREELS). In these HREELS measurements, near-specular scattered electrons due to dipole scattering are captured by a detector in the specular direction. Varying primary beam energy or incident angle corresponds to shifting an probing region on the Q-ω plane (see, e.g., Fig. 1 in ref. 16) and simultaneously to changing the probing depth. Here Q and ω signify surface-parallel wavenumber and angular frequency, respectively. By observing the energy shift and the intensity variation of loss peaks with change of primary beam energy, we can acquire important information about the energy dispersion and the spatial structure of surface excitation modes. These experimental studies by HREELS have encouraged theoretical studies based upon various approaches. Especially, the calculational scheme based upon the RPA is quite effective not only for a surface with a flat band[17-19] but also for a surface with a depletion or accumulation layer.[16,20-22] In the presence of a thick depletion layer, we can introduce a carrier-free depletion layer with adjusted thickness (layer model)[23] and describe the dynamical response of the carrier system below the layer by the RPA scheme.[16] In a further advanced and general approach to a depletion or accumulation layer, we calculate the RPA surface response by using the effective one-particle potential and envelope functions in the ground state or in thermal equilibrium which are obtained from self-consistent calculations.[20-22]

Here, we are concerned with a flat-band case or, at most, a weak band-bending case. As illustrated in Fig. 2, there exist three distinct coupled surface modes at each Q in a smaller but finite Q range, which form three surface dispersion branches. In Fig. 2, the triangular area between two dotted lines shows a probing region in EELS which depends upon primary beam energy and incident angle. A loss peak appears at an energy value where a dispersion branch intersects the probing region. The surface energy-loss intensity decays away on a broken part of each dispersion branch. By choosing an adequate doping level very carefully, these three coupled surface modes have been observed in EEL spectra as three resolved loss peaks.[10] Each of these three modes corresponds to a pole of the surface energy-loss function F_S, which forms a resonance peak in ω dependence of F_S (see Fig. 2 in ref. 19). All the information about surface excitations is included in the expression of the electron energy-loss probability only in the form of F_S.

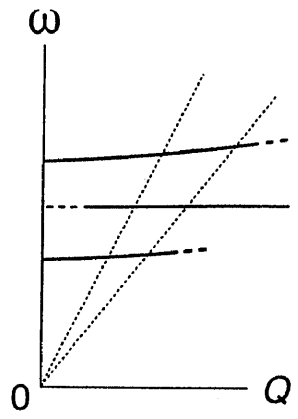

Figure 2. Illustration of energy dispersion of coupled surface modes.

The present report elucidates the coupling character and the spatial structure of each coupled surface mode, the evolution of the character and structure of each mode with change of carrier concentration, and the origin of three coupled surface modes. The induced charge-density distribution in each coupled surface mode is composed of a carrier component $\delta\rho_{EL}$ due to carrier density fluctuation, a phonon component $\delta\rho_{PH}$ originating from longitudinal polar-phonon polarization and an on-surface component σ resulting from termination of the phonon and background polarization at the surface. We can clarify the coupling character of each mode by analyzing the phase relation and the amplitude ratio of these components and by evaluating the contribution of each component to the surface energy-loss intensity. In addition, we can visualize the spatial structure of each mode by drawing contour maps of the induced charge-density distribution and electric field profiles. In n-type polar semiconductors such as n-GaAs, n-InSb and n-InAs, especially in n-InSb, carrier electrons easily become degenerate with increase of carrier concentration, because combination of an extremely small effective mass and a large dielectric constant leads to a large effective Bohr radius, and consequently, to a small effective density parameter. We take a flat-band surface of n-type InSb as an example for calculation. We treat carriers of high effective density as a semi-infinite degenerate carrier-electron gas, and employ the RPA to calculate the dynamical surface response of this carrier system. The RPA is more adequate for an electron gas of higher effective density. We describe the polar-phonon polarization by the Lorentzian oscillator model. This model is appropriate for surface excitation modes whose spatial variation is quite slow on the interatomic scale. The dynamical response of carriers and the polar-phonon polarization interact with each other through the self-consistent electrostatic potential.

Details of the present work have already been given in refs. 19 and 24. The former has explored the structure of three coupled surface modes at a carrier concentration in the strong-coupling regime, and has clarified the origin of the three modes. The latter has examined the structure evolution of the three modes with change of carrier concentration.

2. Theory

We formulate the dynamical response of carrier electrons and the polar-phonon polarization which interact with each other. We describe carriers of

high effective density by a degenerate carrier-electron gas which is restrained in a square-well potential with an infinite barrier at the surface z=0. Here, the z-axis is taken to be normal to the surface, and the material extends in a region z<0. An oscillatory external potential propagating in the surface-parallel direction with surface-parallel wavevector $\boldsymbol{Q}$ and angular frequency ω induces a surface excitation mode specified by the same set of $\boldsymbol{Q}$ and ω. When the external potential is created by external charges outside the material, the external potential U of $\boldsymbol{Q}$ penetrates into the material as e^{Qz}. The surface dielectric response involves induced charges, which generate an induced potential ϕ. The external potential U and the induced potential ϕ add up to the total potential V.

We employ the random-phase approximation (RPA) to describe the dynamical response of the carrier system. The induced charge density $\delta\rho_{EL}$ due to carrier density fluctuation is expressed as

$$\delta\rho_{EL}(z) = \int_{-\infty}^{0} dz' \chi(z,z') V(z'), \tag{1}$$

where the susceptibility $\chi(z, z')$ is given by

$$\chi(z,z') = \frac{4e^2}{\pi^2}\int_0^\infty dk \int_0^\infty dk' S(k,k') \sin(kz') \sin(k'z') \times \sin(k'z) \sin(kz), \tag{2}$$

with

$$S(k,k') = 2\int \frac{d^2K}{(2\pi)^2} \frac{f(\boldsymbol{K}+\boldsymbol{Q},k') - f(\boldsymbol{K},k)}{\varepsilon(\boldsymbol{K}+\boldsymbol{Q},k') - \varepsilon(\boldsymbol{K},k) + \hbar\omega + i\eta}. \tag{3}$$

In these equations, complete forms of $\delta\rho_{EL}(\boldsymbol{Q}, z, \omega)$, $\chi(\boldsymbol{Q}, z, z', \omega)$, $V(\boldsymbol{Q}, z, \omega)$ and $S(\boldsymbol{Q}, k, k', \omega)$, the first three of which are in partially Fourier-transformed representation, are contracted to $\delta\rho_{EL}(z)$, $\chi(z, z')$, $V(z)$ and $S(k, k')$, respectively. In eq. (3), the conduction-band dispersion $\varepsilon(\boldsymbol{K}, k)$ is expressed as

$$\varepsilon(\boldsymbol{K},k) = \left(\hbar^2/2m^*\right)\left(\boldsymbol{K}^2 + k^2\right), \tag{4}$$

with surface-parallel wavevector $\boldsymbol{K}$ and surface-normal wavenumber k, and $f(\boldsymbol{K}, k)$ and η signify the Fermi-Dirac distribution function for conduction-electron states and an infinitesimal positive constant, respectively. From Poisson's equation, we can derive the following expression:

$$V(z) = V(0)e^{Qz} + \frac{1}{\varepsilon_{PH}(\omega)}\frac{2\pi}{Q}\left(\int_{-\infty}^{0} dz' e^{-Q|z'-z|}\delta\rho_{EL}(z') - e^{Qz}\int_{-\infty}^{0} dz' e^{Qz'}\delta\rho_{EL}(z')\right). \tag{5}$$

The polar-phonon and background polarization is included in this equation in the form of the dielectric function

$$\varepsilon_{PH}(\omega) = \varepsilon_\infty\left[1 + \frac{\omega_{PH}{}^2}{\omega_{TO}{}^2 - \omega^2 - i\gamma\omega}\right], \tag{6}$$

where ω_{PH} is given by

$$\omega_{PH}{}^2 = \left[(\varepsilon_0 - \varepsilon_\infty)/\varepsilon_\infty\right]\omega_{TO}{}^2. \tag{7}$$

In eqs. (6) and (7), ω_{TO} is the transverse optical-phonon frequency, ε_∞ and ε_0 are the high-frequency and static dielectric constants in the absence of carriers, respectively, and γ is the phonon relaxation-rate constant. The polar-phonon polarization is described by the Lorentzian oscillator model. We can obtain the z dependence of V and $\delta\rho_{EL}$ by solving eqs. (1) and (5) self-consistently.

The induced potential outside the material (z>0) can be written as

$$\phi(z) = -\frac{\varepsilon_S(\boldsymbol{Q},\omega) - 1}{\varepsilon_S(\boldsymbol{Q},\omega) + 1} U(0) e^{-Qz}, \tag{8}$$

in terms of the surface dielectric function given by

$$\varepsilon_S(\boldsymbol{Q},\omega) = \frac{\varepsilon_{PH}(\omega)}{QV(0)}\left(\frac{\partial}{\partial z}V(z)\right)_{z=-0}. \tag{9}$$

In eq. (8), full forms $\phi(\boldsymbol{Q}, z, \omega)$ and $U(\boldsymbol{Q}, z, \omega)$ are abbreviated as $\phi(z)$ and $U(z)$, respectively. The surface energy-loss function defined by

$$F_S(\boldsymbol{Q},\omega) = \mathrm{Im}\left[-\phi(0)/U(0)\right] = \mathrm{Im}\left[-2/\left\{\varepsilon_S(\boldsymbol{Q},\omega) + 1\right\}\right], \tag{10}$$

describes the intensity of the surface energy loss which occurs in response to the external potential U with $\boldsymbol{Q}$ and ω, where Im denotes the imaginary part.

The induced charge-density distribution is composed of three components:

(a) $\delta\rho_{EL}$, the component due to carrier-density fluctuation.

(b) $\delta\rho_{PH}$, the component originating from the longitudinal polar-phonon polarization. Following the Lorentzian oscillator model, the polar-phonon polarization $\boldsymbol{P}(\boldsymbol{r},\omega)$ is described by

$$\left(\omega_{TO}{}^2 - \omega^2 - i\gamma\omega\right)\boldsymbol{P}(\boldsymbol{r},\omega) = -\left(\varepsilon_\infty/4\pi\right)\omega_{PH}{}^2 \,\mathrm{grad}\, V(\boldsymbol{r},\omega), \tag{11}$$

and this polarization creates the induced charge density

$$\delta\rho_{PH}(\boldsymbol{r},\omega) = -\mathrm{div}\,\boldsymbol{P}(\boldsymbol{r},\omega). \tag{12}$$

(c) σ, the component which arises right on the surface (z=0) owing to termination of the phonon and background polarization at the surface. This component is written as

$$\sigma(\boldsymbol{Q},\omega) = -\frac{\varepsilon_{\rm PH}(\omega)-1}{4\pi}\left(\frac{\partial}{\partial z}V(z)\right)_{z=-0}, \qquad (13)$$

which can be decomposed into the phonon component $\sigma_{\rm PH}$ and the background component $\sigma_{\rm BG}$ as

$$\sigma(\boldsymbol{Q},\omega) = \sigma_{\rm PH}(\boldsymbol{Q},\omega) + \sigma_{\rm BG}(\boldsymbol{Q},\omega). \qquad (14)$$

These components can be expressed as

$$\sigma_{\rm PH}(\boldsymbol{Q},\omega) = -\frac{\varepsilon_{\rm PH}(\omega)-\varepsilon_\infty}{4\pi}\left(\frac{\partial}{\partial z}V(z)\right)_{z=-0}, \qquad (15)$$

and

$$\sigma_{\rm BG}(\boldsymbol{Q},\omega) = -\frac{\varepsilon_\infty-1}{4\pi}\left(\frac{\partial}{\partial z}V(z)\right)_{z=-0}. \qquad (16)$$

By using eqs. (15) and (16), we can examine the phase relation and the amplitude ratio of $\sigma_{\rm PH}$ and $\sigma_{\rm BG}$ in each coupled surface mode.

The induced charge-density distribution $\delta\rho$ inside the material ($z<0$) consists of $\delta\rho_{\rm EL}$ and $\delta\rho_{\rm PH}$ as

$$\delta\rho = \delta\rho_{\rm EL} + \delta\rho_{\rm PH}. \qquad (17)$$

If the x-axis is oriented to the direction of $\boldsymbol{Q}$, we can construct the spatial distribution of $\delta\rho$ in the x-z cross-sectional plane for each surface mode of $\boldsymbol{Q}$ and ω by

$$\delta\rho(x,z) = \delta\rho(\boldsymbol{Q},z,\omega)e^{iQx} + \text{c.c.}, \qquad (18)$$

in terms of $\delta\rho(\boldsymbol{Q},z,\omega)$. The symbol c.c. signifies the complex-conjugate term. We can also build up $\delta\rho_{\rm EL}(x,z)$, $\delta\rho_{\rm PH}(x,z)$, and $\sigma(x)$ in the same manner as in eq. (18). By decomposing $\phi(0)$ ($=V(0)$-$U(0)$) into $\phi_{\rm EL}(0)$, $\phi_{\rm PH}(0)$ and $\phi_{\rm SC}(0)$, we can rewrite the expression of the surface energy-loss function in eq. (10) as

$$F_{\rm S}(\boldsymbol{Q},\omega) = {\rm Im}\left[-\phi_{\rm EL}(0)/U(0)\right] + {\rm Im}\left[-\phi_{\rm PH}(0)/U(0)\right] + {\rm Im}\left[-\phi_{\rm SC}(0)/U(0)\right], \qquad (19)$$

where $\phi_{\rm EL}(0)$ and $\phi_{\rm PH}(0)$ are the induced potentials produced by $\delta\rho_{\rm EL}$ and $\delta\rho_{\rm PH}$, respectively, under screening due to the background polarization ε_∞:

$$\phi_{\rm EL}(0) = \frac{1}{\varepsilon_\infty}\frac{2\pi}{Q}\int_{-\infty}^{0}dz'e^{Qz'}\delta\rho_{\rm EL}(z'), \qquad (20)$$

$$\phi_{\rm PH}(0) = \frac{1}{\varepsilon_\infty}\frac{2\pi}{Q}\int_{-\infty}^{0}dz'e^{Qz'}\delta\rho_{\rm PH}(z'). \qquad (21)$$

The induced-potential component $\phi_{\rm SC}(0)$ is generated by σ as

$$\phi_{\rm SC}(0) = (2\pi/Q)\sigma(\boldsymbol{Q},\omega). \qquad (22)$$

Plotting $\phi_{\rm EL}(0)/U(0)$, $\phi_{\rm PH}(0)/U(0)$ and $\phi_{\rm SC}(0)/U(0)$ on the complex plane serves to understand the phase relation of $\delta\rho_{\rm EL}$, $\delta\rho_{\rm PH}$ and σ in variation along x and the contribution of each induced charge component to the surface energy-loss intensity.[19,24]

3. Analysis

Our calculation is concerned with an n-type InSb flat-band surface. The conduction-band dispersion of InSb is almost isotropic, but highly nonparabolic. We incorporate this nonparabolicity into our calculation by taking the effective mass $m_{\rm F}^*$ defined at the Fermi wavenumber $k_{\rm F}$ by

$$\frac{1}{m_{\rm F}^*} = \frac{1}{\hbar^2 k_{\rm F}}\left(\frac{{\rm d}E(k)}{{\rm d}k}\right)_{k=k_{\rm F}}, \qquad (23)$$

where the conduction-band dispersion $E(k)$ can be calculated by Kane's scheme (see eq. (10) in ref. 25). In our calculation, we ignore the temperature effect around the Fermi level and assume the T=0 step function for the Fermi-Dirac distribution function in eq. (3). This enables us to calculate the K-integral in eq. (3) analytically. In the case of n-type InSb, the temperature effect is modest if temperature is not so high, because the Fermi energy becomes considerably high in the strong-coupling concentration regime because of an extremely small effective mass. The above incorporation of the nonparabolicity is a good approximation for excitation modes whose wavenumbers are small compared with $k_{\rm F}$. The effective mass $m_{\rm F}^*$ in eq. (23) is employed as m^* in section 2. Table 1 in ref. 5 compiles values of the effective mass $m_{\rm F}^*$ and the effective density parameter $r_{\rm S}^*$ at various carrier concentrations. Other parameter values are taken to be ε_0=17.88, ε_∞=15.68, $\hbar\omega_{\rm TO}$=22.90 meV and $\gamma/\omega_{\rm TO}$=0.007.[26]

Figure 3 exhibits the carrier-density profile near the surface in the ground state which is normalized by the bulk carrier density. The vertical z-axis is scaled by $k_{\rm F}^{-1}$. By referring to this figure in investigating each surface excitation mode, we can realize how induced charges are distributed on the

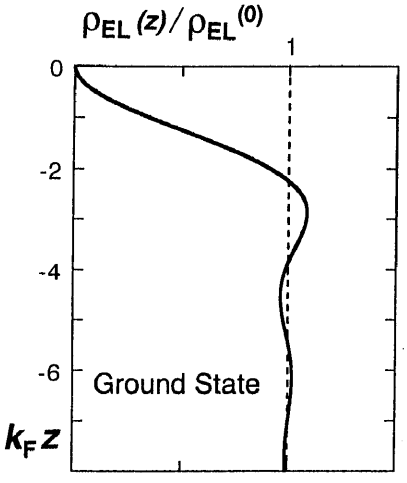

Figure 3. Carrier density profile near the surface in the ground state. $\rho_{\rm EL}(z)$ and $\rho_{\rm EL}^{(0)}$ signify the carrier charge density at depth z and that in the bulk, respectively.

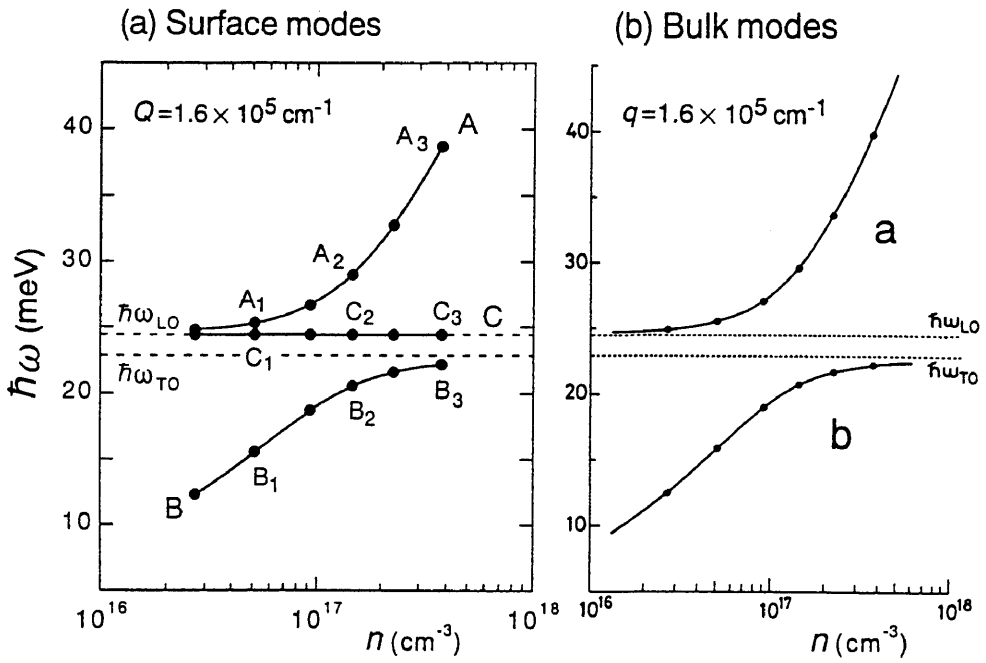

Figure 4. Carrier-concentration dependence of energy values of (a) three coupled surface modes at $Q=1.6\times10^5$ cm^{-1} and (b) two coupled bulk modes at $q=1.6\times10^5$ cm^{-1}.

carrier-density profile curve in the ground state.

At each carrier concentration, we explore surface resonance modes at chosen Q which correspond to peaks in ω dependence of F_S. As mentioned in section 1, there exist three distinct coupled surface modes at each Q in a smaller but finite Q range. Figure 4(a) displays the carrier-concentration dependence of energy values of the three coupled surface modes at $Q=1.6\times10^5$ cm^{-1}. The abscissa is indicated in logarithmic scale. The energy of the intermediate mode C is almost equal to the longitudinal optical-phonon energy $\hbar\omega_{LO}=\sqrt{\varepsilon_0/\varepsilon_\infty}\,\hbar\omega_{TO}=24.45$ meV irrespective of carrier concentration n. This mode is identified as the surface optical-phonon mode which undergoes screening due to presence of carriers. In the absence of carriers, the surface optical-phonon mode has its energy at $\hbar\omega=\left[(\varepsilon_0+1)/(\varepsilon_\infty+1)\right]^{1/2}\hbar\omega_{TO}=24.36$meV, which is just below $\hbar\omega_{LO}=24.45$ meV. The energy of the upper mode A approaches $\hbar\omega_{LO}$ with decrease of n, while the energy of the lower mode B becomes closer to $\hbar\omega_{TO}$ with increase of n. The energy variation of the modes A and B originates from strong plasmon-phonon coupling which occurs when the surface-plasmon energy intersects the phonon energy regime. Therefore, the modes A and B become plasmon-like well above and below the strong-coupling concentration regime, respectively. Figure 4(b) shows the energy values of the two coupled *bulk* modes at wavenumber $q=1.6\times10^5$ cm^{-1} for the same set of n. This value of q is the same as the above value of surface-parallel wavenumber Q. The symbols a and b denote the modes on the dispersion branches a and b in Fig. 1, respectively. These bulk modes are also calculated by using the RPA scheme combined with the Lorentzian oscillator model. By comparing Fig. 4(a) with Fig. 4(b), we notice that there is only a slight or almost no difference between the surface-mode energy and the bulk-mode energy. This can be understood by considering a few simple cases. As stated above, in the absence of carriers, the surface phonon frequency is given by $\omega_S=[(\varepsilon_0+1)/(\varepsilon_\infty+1)]^{1/2}\omega_{TO}$, which is very close to the bulk phonon frequency $\omega_{LO}=(\varepsilon_0/\varepsilon_\infty)^{1/2}\omega_{TO}$ because of the relation $1<<\varepsilon_\infty<\varepsilon_0$. In the absence of phonon ($\omega_{PH}=0$), the surface plasmon frequency at $Q=0$ is expressed as $\omega_S=[\varepsilon_\infty/(\varepsilon_\infty+1)]^{1/2}\Omega_{PL}$, which is quite close to Ω_{PL}, namely, the bulk plasmon frequency at $q=0$. In the case of semiconductors, the surface-mode energy is only slightly lower than or almost the same as the bulk-mode energy, because of high background polarization ε_∞.

Figures 5-11 display the coupling character and the spatial structure of those coupled surface modes at $Q=1.6\times10^5$ cm^{-1} which are labeled as A_i, B_i, and C_i in Fig. 4(a) with subscripts i(=1, 2, 3) indicating carrier concentration. Figs. 5 and 6, Figs. 7-9 and Figs. 10 and 11 are relevant to the modes A, B and C, respectively. Figures 5, 7 and 10 show the variation of $\sigma_{BG}(x)$ and $\sigma_{PH}(x)$ and the contour maps of $\delta\rho_{EL}(x,z)$ and $\delta\rho_{PH}(x,z)$ in the modes A_2, B_2 and C_2, respectively. Figures 6, 8 and 11 exhibit the contour maps of $\delta\rho(x,z)$ in the modes A_i, B_i, and C_i, (i=1,3), respectively. Figure 9 displays the total electric-field profile in the modes B_1 and B_3. The total electric field is obtained from gradient of the total electrostatic potential V.

We examine the coupling character and the spatial structure of each coupled surface mode at various carrier concentrations n. First, we explore the higher-energy mode A. In this mode, all of $\delta\rho_{EL}$, $\delta\rho_{PH}$ and σ cooperate to enhance the surface energy-loss intensity, and $\delta\rho_{EL}(x,z)$ is in coherent-phase relation with $\delta\rho_{PH}(x,z)$ in variation along x (see Fig. 5). The two components σ_{BG} and σ_{PH} are

π radian out of phase with each other in variation along x, and the background component σ_{BG} has a larger amplitude. This is the coupling character of the higher-energy mode A regardless of n. Above the strong-coupling concentration regime, $\delta\rho_{EL}$ makes a dominant contribution to $\delta\rho$, and with decrease of n, the contribution of $\delta\rho_{EL}$ becomes less and less predominant over that of $\delta\rho_{PH}$, and below the strong-coupling regime, $\delta\rho_{PH}$ begins to make more contribution. This remarkable change in relative contribution of $\delta\rho_{EL}$ and $\delta\rho_{PH}$ implies the evolution from plasmon to phonon character with decrease of n. As displayed in Figs. 5 and 6, the main structure in contours of $\delta\rho(x,z)$ is an alternating sequence of a high mountain and a deep hollow which lies in a surface region $k_F|z| \lesssim 3$. The vertical scale in Fig. 6(a) is enlarged compared with that in Fig. 5 or 6(b). In view of the carrier-density profile in the ground state drawn in Fig. 3, we find that this main structure is formed right in the surface region where the carrier density ρ_{EL} drops and vanishes. The wavy feature in contours of $\delta\rho(x,z)$ originates from the interference of electronic waves incident on and reflected from the surface. Here, we follow the variation of the spatial structure with decrease of n, namely, from the mode A_3 to the mode A_1. The energy of the mode A_3 is well above the phonon energy regime, and plasmon character is dominant in this mode. As exhibited in Fig. 6(b), each high mountain or each deep hollow in the main structure extends a long wavy skirt into the deeper region. This extending feature into the deeper region originates from the fact that the surface-plasmon energy is slightly below the bottom of projected bulk plasmon bands owing to high background polarization ε_∞. The induced surface charges σ arise mainly from termination of the background polarization ε_∞ at the surface. The carrier component $\delta\rho_{EL}$ plays the leading role in the mode A_3. As phonon character becomes more influential with decrease of n, the wavy extending skirts in $\delta\rho(x,z)$ become less and less conspicuous, and below the strong-coupling regime, these skirts dwindle away to remnant short-range features. In the mode A_1, $\delta\rho_{PH}$ makes the main contribution to $\delta\rho$, and $\delta\rho_{EL}$ operates to augment $\delta\rho$ on account of the coherent phase relation. The amplitude of σ_{PH} becomes comparable to that of σ_{BG}, and the anti-phase relation of σ_{BG} and σ_{PH} in variation along x operates to reduce the amplitude of σ. The phonon component $\delta\rho_{PH}$ plays the leading role in the mode A_1, which is consistent with the fact the mode energy is just above $\hbar\omega_{LO}$. Some distorted feature of the contour pattern in the surface region $k_F|z| \lesssim 3$ (see Fig. 6(a)) could be understood by considering that propagation of this mode is driven by the strong electric-field flux which flows from each high mountain of $\delta\rho$ to its neighboring deep hollows of $\delta\rho$ through the deeper region.

Secondly, we analyze the lower-energy mode B. Both of $\delta\rho_{EL}$ and σ operate to enhance the surface energy-loss intensity, while $\delta\rho_{PH}$ acts to suppress it. The variation of $\delta\rho_{EL}(x,z)$ along x is in anti-phase relation with that of $\delta\rho_{PH}(x,z)$ along x, and $\delta\rho_{EL}$ makes more contribution to $\delta\rho$ (see Fig. 7). The two components σ_{BG} and σ_{PH} are in phase with each other in variation along x. This is the coupling character of the mode B irrespective of n. Above the strong-coupling concentration regime, $\delta\rho_{EL}$ and $\delta\rho_{PH}$ tend to cancel out each other, though $\delta\rho_{EL}$ survives, and with decrease of n, the contribution of $\delta\rho_{EL}$ becomes more and more predominant over that of $\delta\rho_{PH}$, and finally $\delta\rho_{EL}$ begins to make a dominant contribution to $\delta\rho$. This change in relative contribution of $\delta\rho_{EL}$ and $\delta\rho_{PH}$ implies the transformation to plasmon character. As shown in Figs. 7 and 8, the main structure in contours of $\delta\rho(x,z)$ is an alternating array of a high mountain and a deep hollow in the surface region $k_F|z| \lesssim 3$, and each mountain or hollow has a long wavy skirt extending into the deeper region. As in the mode A, the main structure is formed right in the surface layer where the ground-state carrier density ρ_{EL} falls and vanishes. Below the strong-coupling regime, the mode B becomes plasmon-like, and the carrier component $\delta\rho_{EL}$ plays the leading role. The background component σ_{BG} makes the main contribution to σ. Although plasmon character declines with increase of n, the wavy extending feature in contours of $\delta\rho(x,z)$ persists even above the strong-coupling concentration regime, namely, in the mode B_3. This persistence can be ascribed to the fact that regardless of n, $\delta\rho_{EL}$ continues to make more contribution to $\delta\rho$, though $\delta\rho_{EL}$ and $\delta\rho_{PH}$ tend to cancel out each other above the strong-coupling regime. The phonon component σ_{PH} makes the main contribution to σ, and the background component σ_{BG} cooperates with σ_{PH} to enhance σ owing to the coherent-phase relation. The phonon component σ_{PH} plays the leading role in the mode B_3. Significance of σ in this mode reveals itself in the total electric-field profile which shows the prominent transverse flux issuing from or terminating at the surface (see Fig. 9(b)). The variation of σ along x remarkably departs from the exact coherent-phase relation with that of $\delta\rho$ along x. The above transverse flux is in sharp contrast to the longitudinal flux which is dominant in the total electric-field profile of the mode B_1 (see Fig. 9(a)). Some distorted feature in contours of $\delta\rho(x,z)$ in the surface region $k_F|z| \lesssim 3$ in the mode B_3 could be understood by considering that the induced surface charges σ lead propagation of this mode.

Lastly, we investigate the intermediate-energy mode C. This mode is identified as the surface optical-phonon mode which suffers the screening effect due to existence of carriers. In the absence of carriers, the surface optical-phonon mode has its induced changes only at the surface (z=0), and these induced surface charges σ solely contribute to the surface energy-loss intensity. In the presence of carriers, however, there occur induced charges $\delta\rho$ in the material also. Although occurrence of $\delta\rho$ originates from existence of carriers, it is not $\delta\rho_{EL}$ but $\delta\rho_{PH}$ that makes the major contribution to $\delta\rho$. The polar phonon plays the leading role in this mode. The induced charge component $\delta\rho$ operates against σ to reduce the surface energy-loss intensity. This implies that the induced internal charges $\delta\rho$ have the screening effect on the surface optical phonon dominated by the induced surface charges σ. At higher carrier concentration, this screening

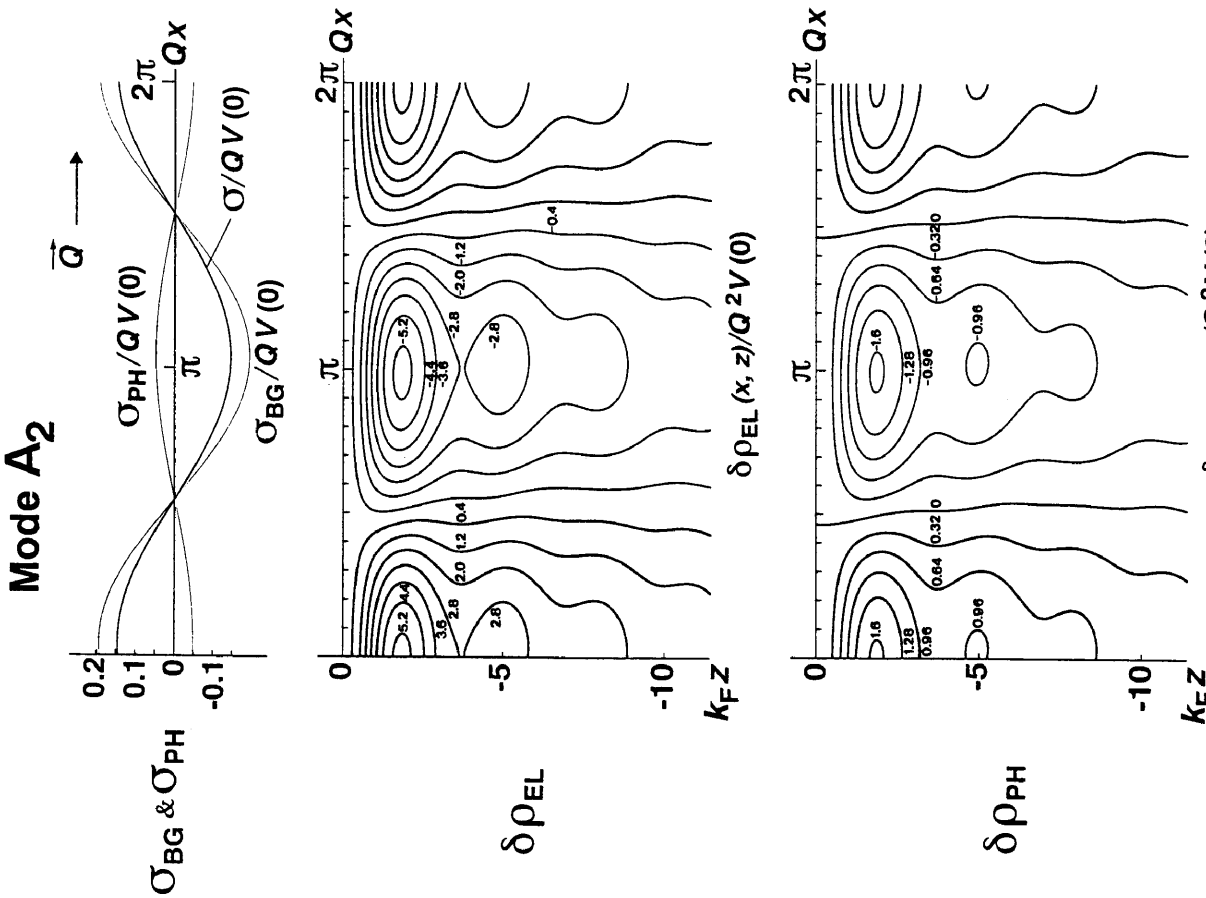

Figure 5. Variation of $\sigma_{BG}(x)$ and $\sigma_{PH}(x)$ and contour maps of $\delta\rho_{EL}(x,z)$ and $\delta\rho_{PH}(x,z)$ of the mode A_2.

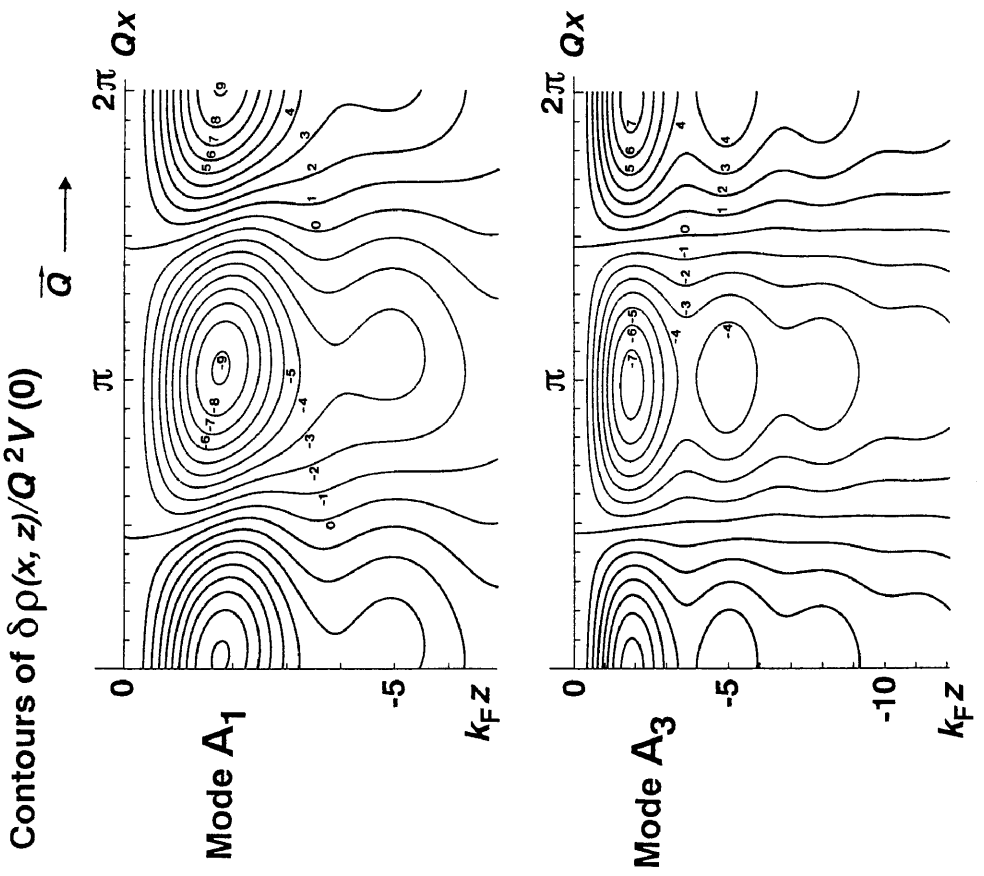

Figure 6. Contour maps of $\delta\rho(x,z)$ of the modes A_1 and A_3. Adapted from Fig. 4 in ref. 24.

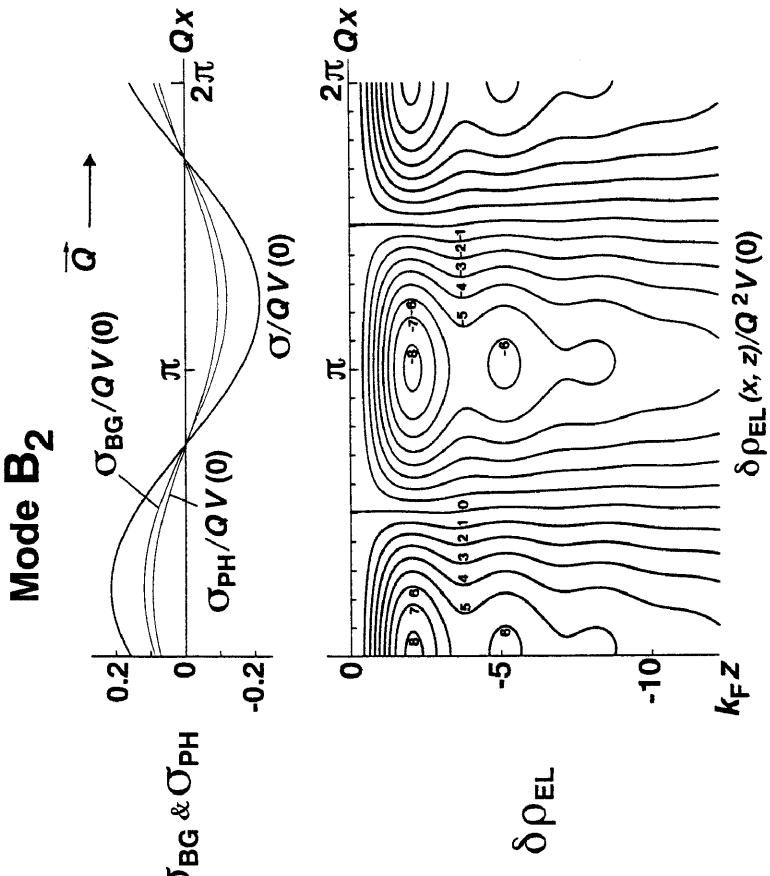

Figure 7. Variation of $\sigma_{BG}(x)$ and $\sigma_{PH}(x)$ and contour maps of $\delta\rho_{EL}(x,z)$ and $\delta\rho_{PH}(x,z)$ of the mode B_2.

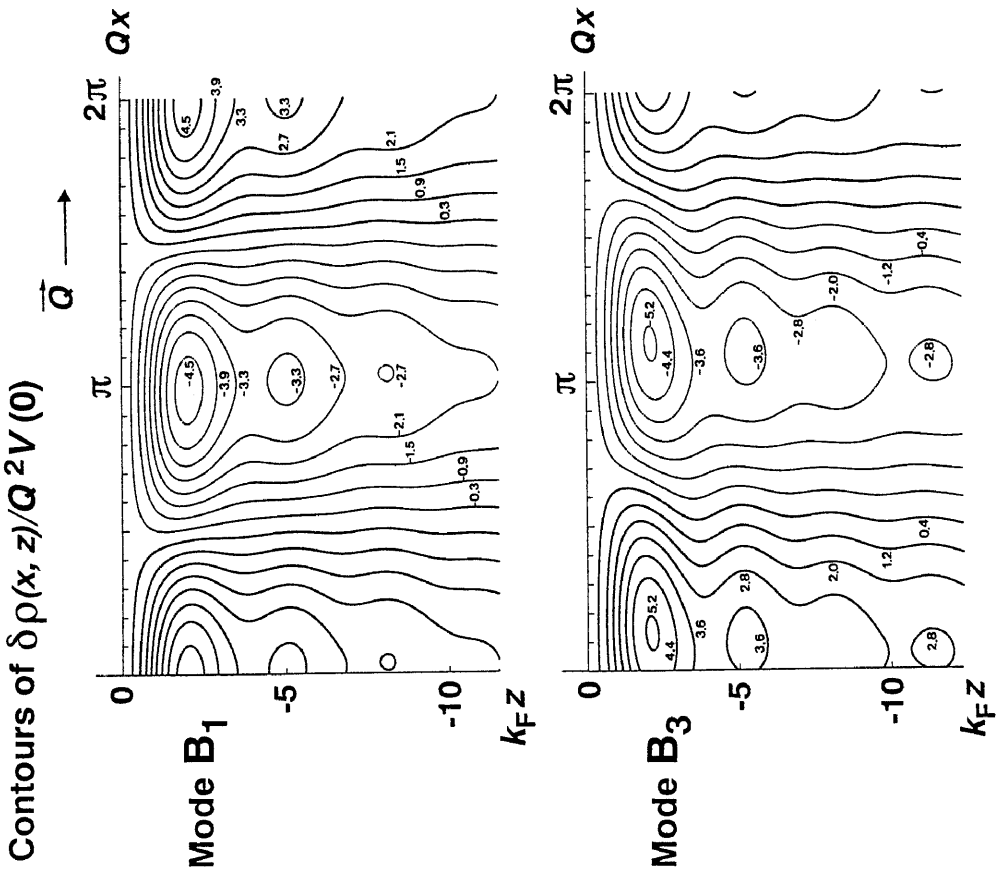

Figure 8. Contour maps of $\delta\rho(x,z)$ of the modes B_1 and B_3. Adapted from Fig. 7 in ref. 24.

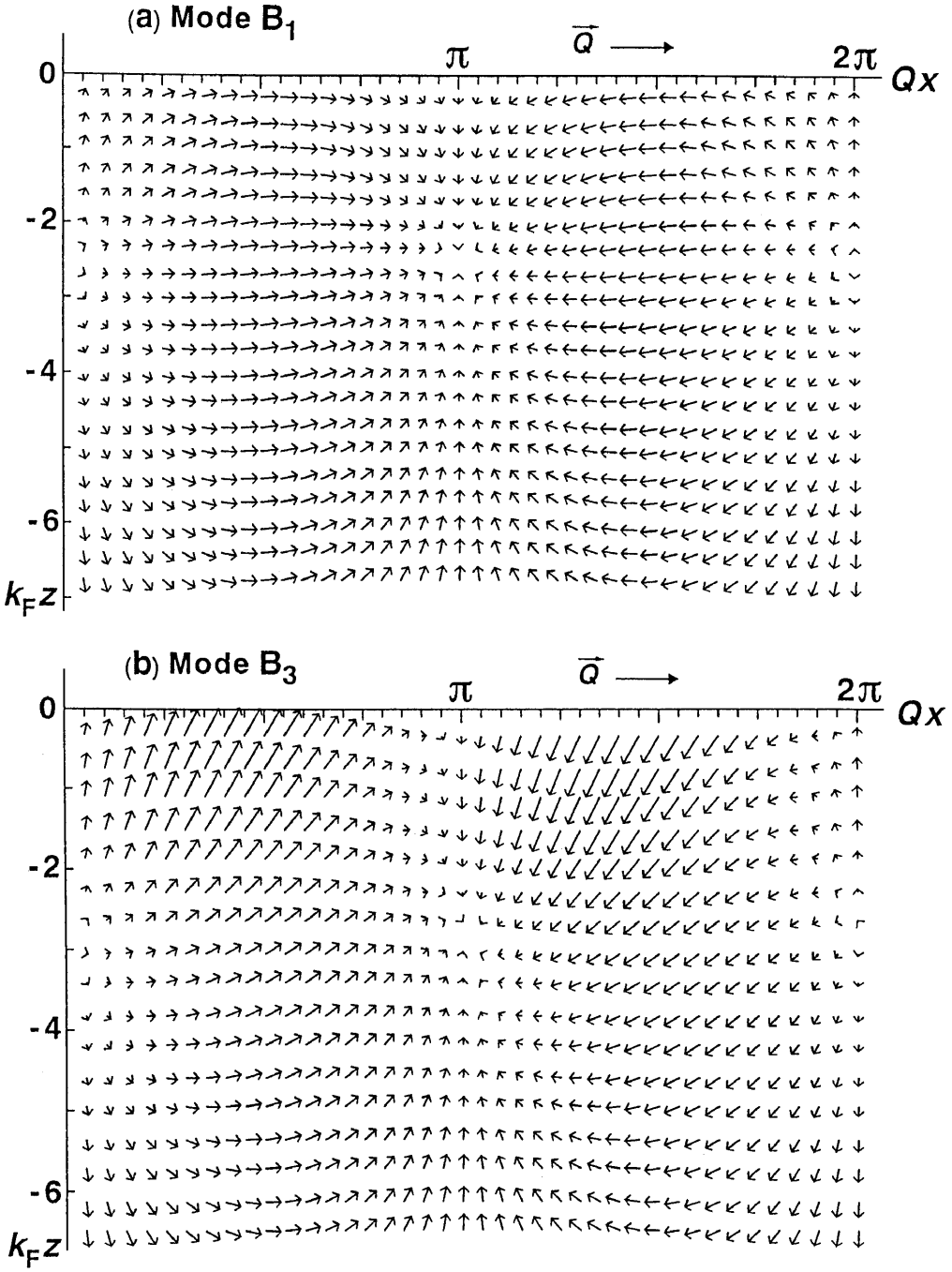

Figure 9. Total electric-field profiles of the modes B_1 and B_3. Adapted from Fig. 8 in ref. 24.

operates more effectively to reduce the surface energy-loss intensity. The contour maps in Fig. 10 show a localized feature of the mode C. The Thomas-Fermi screening length is evaluated to be 2.48 in units of k_F^{-1} for the carrier concentration of the mode C_2. Accordingly, the mode C is localized in a surface region whose thickness is comparable to the Thomas-Fermi screening length. Contour lines of $\delta\rho(x,z)$ exhibit significant tails streaming in the opposite direction to $\boldsymbol{Q}$. These streaming tails indicate that the surface optical phonon propagates along the surface dragging the internal screening charges $\delta\rho$. As shown in Fig. 11, this dragging feature becomes more conspicuous at higher carrier concentration. The variation of σ_{PH} along x is nearly in anti-phase relation with that of σ_{BG} along x. The effective cancellation between σ_{PH} and σ_{BG} operates to reduce σ, and consequently the surface energy-loss intensity, as exhibited below in Fig. 12.

Here, we mention the phase relation of the induced internal charges $\delta\rho$ and the component of σ which survives after canceling out the external potential.[24] In the modes A and B, the variation of $\delta\rho$ along x is in coherent-phase relation with that of the surviving component of σ along x. On the other hand, in the mode C, the variation of $\delta\rho$ along x is in anti-phase relation with that of the surviving component of σ along x.

Our calculational scheme takes no account of collision damping of carriers due to impurities, acoustic phonons, etc. Therefore, energy broadening of a resonance peak of F_S originates from the polar phonon whose damping is described by the relaxation-rate constant γ and from single-particle excitations in the carrier-electron gas. In our case of smaller Q, the former is more effective to

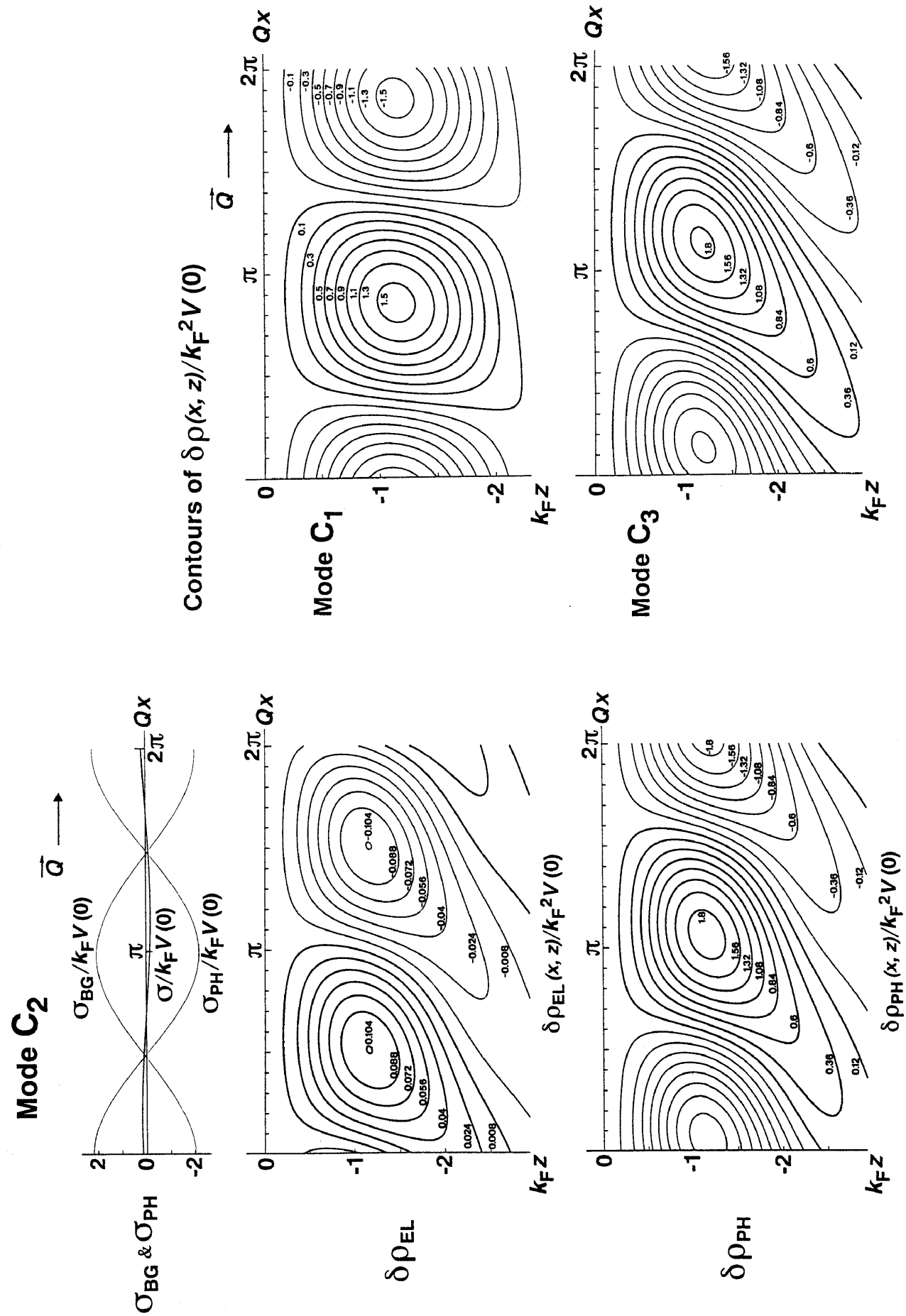

Figure 10. Variation of $\sigma_{BG}(x)$ and $\sigma_{PH}(x)$ and contour maps of $\delta\rho_{EL}(x,z)$ and $\delta\rho_{PH}(x,z)$ of the mode C_2.

Figure 11. Contour maps of $\delta\rho(x,z)$ of the modes C_1 and C_3. Adapted from Fig. 10 in ref. 24.

energy broadening, and plasmon-like modes such as A_3 and B_1 in Fig. 4(a) have sharper resonance peaks. As a quantity independent of this energy broadening, we introduce the area of a resonance peak in ω dependence of F_S, namely, the integrated resonance intensity I defined by

$$I = \int_{\text{peak}} F_S(Q, \omega) \mathrm{d}(\hbar\omega). \tag{24}$$

Figure 12(a) shows the n dependence of I of the three modes, A, B and C. The abscissa and the ordinate are both indicated in logarithmic scale. Each series of six circles in this figure corresponds to one of three series of six circles in Fig. 4(a), respectively. As the mode A transforms its character from plasmon to phonon with decrease of n, the resonance intensity I decreases monotonically and somewhat more significantly in the strong-coupling concentration regime. Above the strong-coupling regime, the mode B has very weak resonance intensity I because of the significant cancellation between $\delta\rho_{EL}$ and $\delta\rho_{PH}$. As the energy of the mode A becomes lower with decrease of n, the mode B becomes coupled with the mode A more strongly, acquires more plasmon character, and gains stronger resonance intensity I. However, the resonance intensity I begins to decline with further decrease of n, when plasmon character is established. As seen by comparing Fig. 12(a) with Fig. 12(b), the n dependence of the resonance intensity I of the modes A and B at $Q=1.6\times10^5$ cm^{-1} is similar to that of the resonance intensity I of the two coupled *bulk* modes at $q=1.6\times10^5$ cm^{-1}. The symbols a and b in Fig. 12(b) signify the modes on the dispersion branches a and b in Fig. 1, respectively. The intensity I for bulk modes is defined by

$$I = \int_{\text{peak}} \mathrm{Im}\left[-1/\varepsilon_B(q, \omega)\right] \mathrm{d}(\hbar\omega), \tag{25}$$

in terms of the bulk dielectric function $\varepsilon_B(q,\omega)$.[5] The above similarity is consistent with the fact that the surface modes A and B are associated with two bulk dispersion branches a and b, respectively, as stated below. With increase of n, the mode C gradually reduces its resonance intensity I, because the screening due to existence of carriers operates more effectively. Significant cancellation between σ_{PH} and σ_{BG} tends to suppress the resonance intensity I. From Figs. 12(a) and 4(a), we can deduce that far above the strong-coupling concentration regime, the mode A will still enhance its resonance intensity I, while the mode B will lose its resonance intensity I quickly, and furthermore the energy separation between the modes B and C will be only about 2 meV. This deduction is compatible with the experimental result that there appear only two loss peaks in EEL spectra of a heavily n-doped InSb (110) cleaved surface, one of which has strong intensity well above the phonon energy regime, and the other of which has weak intensity just near $\hbar\omega_{LO}$.[12] The carrier concentration of the sample in ref. 12 is correctly evaluated to be $n=1.4\times10^{18}$ cm^{-3} by taking account of the nonparabolicity of the conduction-band dispersion.[27] If n is well below the strong-coupling concentration regime, it becomes difficult to resolve the modes A and C in EEL spectra and the loss peak of the mode B may be buried in the tail of the elastic-scattering peak. In order to resolve the three coupled surface modes distinctly, we have to choose an adequate doping level very carefully, and observe with sufficient energy resolution, as is performed for an n-GaAs (110) cleaved surface in ref. 10.

The semi-classical scheme[28] is very helpful to understand existence of the three distinct coupled surface modes. In this scheme, the surface dielectric function $\varepsilon_S(Q,\omega)$ is obtained by integrating the bulk dielectric function $\varepsilon_B(q,\omega)$ with respect to surface-

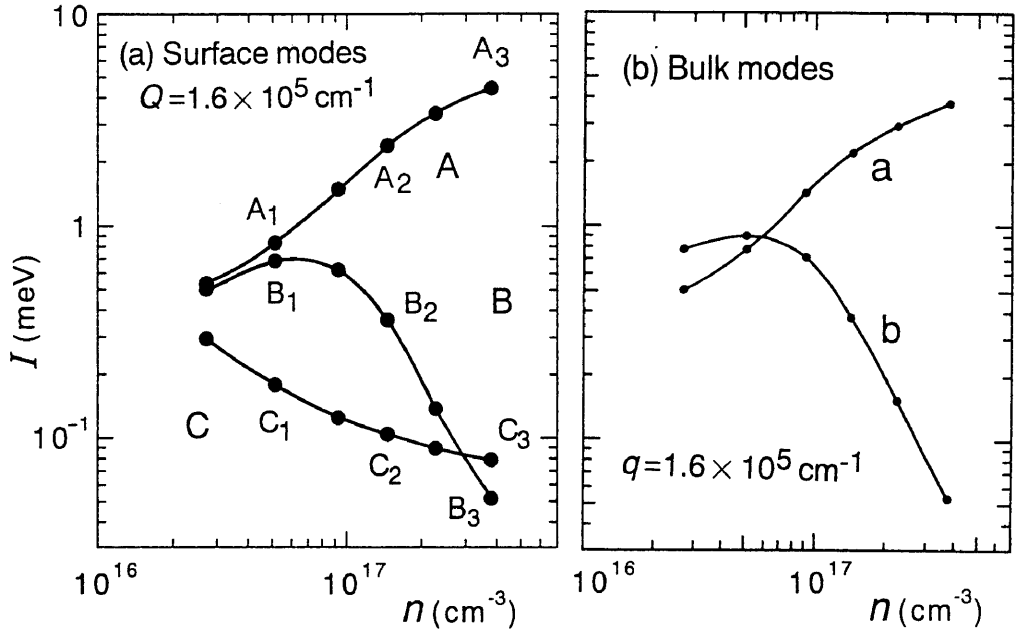

Figure 12. Carrier-concentration dependence of the integrated energy-loss intensity I of (a) three coupled *surface* modes A, B and C at $Q=1.6\times10^5$ cm^{-1} and (b) two coupled *bulk* modes at $q=1.6\times10^5$ cm^{-1} on the dispersion branches a and b in Fig. 1

normal wavenumber q_z:

$$\frac{1}{\varepsilon_S(Q,\omega)} = \frac{2}{\pi}\int_0^\infty dq_z \frac{Q}{Q^2+q_z^2}\cdot\frac{1}{\varepsilon_B(q,\omega)}, \qquad (26)$$

where wavenumber q is given by

$$q = \left(Q^2+q_z^2\right)^{1/2}. \qquad (27)$$

Equation (26) asserts that the surface mode with Q is associated with a large number of bulk modes with $q \geq Q$, because presence of the surface violates the translational symmetry in the surface-normal direction. Figure 1 exhibits the three dispersion branches of coupled bulk modes. In coupled bulk modes on the branch a, $\delta\rho_{EL}$ is in phase with $\delta\rho_{PH}$ in variation along the propagating direction, which is the same coupling character as in the coupled surface mode A. In coupled bulk modes on the branch b, $\delta\rho_{EL}$ is π radian out of phase with $\delta\rho_{PH}$ in variation along the propagating direction, and the former component has a larger amplitude than the latter one. This is the same coupling character as in the coupled surface mode B. As shown in Fig. 4, energy values of the surface mode A and B at $Q=1.6\times10^5$ cm^{-1} are very close to those of the bulk modes at $q=1.6\times10^5$ cm^{-1} on the branches a and b, respectively, throughout the whole range of n. In coupled bulk modes on the branch c, $\delta\rho_{PH}$ makes a dominant contribution to $\delta\rho$ as in the coupled surface mode C. With increase of q, the mode energy of the branch c approaches $\hbar\omega_{LO}$ asymptotically, which forms a remarkably high density of states of bulk resonance modes around $\hbar\omega_{LO}$. Moreover, the mode on the branch c gains stronger resonance intensity I as q becomes larger, because the screening due to carriers operates less effectively. These effects surpass the effect of the Lorentzian weight function in eq. (26) which operates to suppress the contribution from bulk modes in the larger q region. Consequently, bulk phonon modes around $\hbar\omega_{LO}$ with larger q make a dominant contribution to the surface mode C, which leads to a flat surface dispersion branch with its energy very close to $\hbar\omega_{LO}$. After all, from these observations, it follows that each of the three coupled surface modes is associated with one of the three bulk dispersion branches.

4. Summary

Firstly, we have examined the coupling character and the spatial structure of each of the three coupled surface modes with change of carrier concentration n. The induced internal charge density $\delta\rho$ consists of the carrier component $\delta\rho_{EL}$ due to carrier density fluctuation and the phonon component $\delta\rho_{PH}$ originating from longitudinal polar-phonon polarization. The induced surface charge density σ is composed of the background component σ_{BG} arising from termination of the background polarization at the surface and the phonon component σ_{PH} resulting from termination of the polar-phonon polarization at the surface. The x-axis is oriented to the direction of surface-parallel wavevector $\boldsymbol{Q}$, and the z-axis is taken to be normal to the surface so that the material spreads in the region $z<0$. The surface energy-loss function $F_S(\boldsymbol{Q},\omega)$ describes the intensity of the surface energy loss which occurs in response to the external potential of $\boldsymbol{Q}$ and ω, and the integrated resonance intensity I is defined as the area of a resonance peak in ω dependence of F_S. Our results are summarized as follows:

(a) Higher-energy mode A

The variation of $\delta\rho_{EL}(x,z)$ along x is in coherent-phase relation with that of $\delta\rho_{PH}(x,z)$ along x, while the variation of $\sigma_{BG}(x)$ is in anti-phase relation with that of $\sigma_{PH}(x)$, and the former component $\sigma_{BG}(x)$ has a larger amplitude. All of $\delta\rho_{EL}$, $\delta\rho_{PH}$ and σ cooperate to enhance the surface energy-loss intensity. The main structure in contours of $\delta\rho(x,z)$ is an alternating series of a high mountain and a deep hollow in the surface layer where the ground-state carrier density drops and vanishes. This is the coupling character and the spatial structure of mode A irrespective of n. Above the strong-coupling concentration regime, the mode energy is well above the phonon energy regime, the carrier-density fluctuation yielding $\delta\rho_{EL}$ plays the leading role, and plasmon character becomes dominant. Each high mountain or deep hollow in contours of $\delta\rho(x,z)$ extends a long wavy skirt into the deeper region. The background component σ_{BG} makes a dominant contribution to σ. With decrease of n, the mode energy decreases toward $\hbar\omega_{LO}$, and simultaneously there occurs a significant variation in relative contribution of $\delta\rho_{EL}$ and $\delta\rho_{PH}$ which implies the transformation from plasmon to phonon character. Below the strong-coupling regime, the longitudinal polar-phonon polarization producing $\delta\rho_{PH}$ begins to play the leading part, and the effective cancellation between σ_{BG} and σ_{PH} operates to suppress the amplitude of σ. With decrease of n, the wavy extending skirts in contours of $\delta\rho(x,z)$ become less and less conspicuous, and below the strong-coupling regime, these skirts dwindle and disappear. As n becomes smaller, the resonance intensity I decreases monotonically and somewhat more significantly in the strong-coupling concentration regime.

(b) Lower-energy mode B

The variation of $\delta\rho_{EL}(x,z)$ along x is in anti-phase relation with that of $\delta\rho_{PH}(x,z)$ along x, and the former one has a larger amplitude. On the other hand, the variation of $\sigma_{BG}(x)$ is coherent with that of $\sigma_{PH}(x)$. Both $\delta\rho_{EL}$ and σ operate to enhance the surface energy-loss intensity, while $\delta\rho_{PH}$ acts to reduce it. As in the mode A, the main structure in contours of $\delta\rho(x,z)$ is constructed by an alternating array of a high mountain and a deep hollow in the surface region where the ground-state carrier density falls and vanishes. Each high mountain or deep hollow has a long wavy skirt extending into the deeper region. This is the coupling character and the spatial structure of mode B independent of n. Below the strong-coupling concentration regime, this mode becomes plasmon-like, and the carrier component $\delta\rho_{EL}$ plays the leading role as in the mode A above the strong-coupling regime. The background component σ_{BG} makes the major

contribution to σ. As the mode energy increases toward $\hbar\omega_{TO}$ with increase of n, the contribution of $\delta\rho_{EL}$ becomes less and less predominant over that of $\delta\rho_{PH}$, and above the strong-coupling regime, $\delta\rho_{EL}$ and $\delta\rho_{PH}$ tend to cancel out each other. Although plasmon character declines with increase of n, the wavy extending feature in contours of $\delta\rho(x,z)$ persists to above the strong-coupling regime, because $\delta\rho_{EL}$ continues to make more contribution to $\delta\rho$. Above the strong-coupling regime, the effective cancellation between $\delta\rho_{EL}$ and $\delta\rho_{PH}$ operates to reduce $\delta\rho$, and the induced surface charges σ start to play an important role. The phonon component σ_{PH} makes the major contribution to σ, and the background component σ_{BG} operates to increase σ because of the coherent-phase relation of σ_{PH} and σ_{BG}. As n decreases into the strong-coupling concentration regime, the mode B acquires more plasmon character and gains stronger resonance intensity I. However, the resonance intensity I begins to decline with further decrease of n, once plasmon character is established.

(c) Intermediate-energy mode C

The mode C is identified as the surface optical-phonon mode which undergoes screening due to presence of carriers. The induced surface charges σ operate to enhance the surface energy-loss intensity, while the induced internal charges $\delta\rho$ act to suppress it. This indicates that $\delta\rho$ operates to screen the surface optical phonon dominated by σ. Although occurrence of $\delta\rho$ originates from presence of carriers, it is not $\delta\rho_{EL}$ but $\delta\rho_{PH}$ that makes the dominant contribution to $\delta\rho$. Because of this screening, the mode C is localized in a surface region whose thickness is comparable to the Thomas-Fermi screening length of carriers. At higher n, the screening operates more effectively to reduce the surface energy-loss intensity. The contour map of $\delta\rho(x,z)$ indicates that in this mode, the surface optical phonon propagates along the surface dragging internal screening charges $\delta\rho$. This dragging feature becomes more conspicuous at higher n. Effective cancellation between σ_{PH} and σ_{BG} operates to reduce σ, and consequently the surface energy-loss intensity.

Secondly, the origin of the three coupled surface modes has been clarified by combining the above results with analysis of coupled bulk modes. There exist three dispersion branches of coupled bulk modes. By analyzing the coupling character and the relation between surface modes and bulk dispersion branches, we find that each of the three coupled surface modes is associated with one of the three dispersion branches of coupled bulk modes.

Acknowledgements

The author thanks H. Ojima for her assistance in preparing the manuscript and figures. Numerical calculations in this work were carried out at the Iwate University Computer Center.

1) W. Richter, in: Polarons and Excitons in Polar Semiconductors and Ionic Crystals, Eds. J. T. Devreese and F. Peeters (Plenum, New York, 1984) p. 209 and references therein.
2) G. Abstreiter, M. Cardona and A. Pinczuk, in: Light Scattering in Solids IV, Eds. M. Cardona and G. Güntherodt (Springer, Berlin, 1984) p. 5 and references therein.
3) S. Katayama, K. Murase and H. Kawamura, Solid State Commun. **16** (1975) 945.
4) L. F. Lemmens, F. Brosens and J. T. Devreese, Solid State Commun. **17** (1975) 337.
5) T. Inaoka, J. Phys. Condensed Matter **3** (1991) 4825.
6) N. Mori and T. Ando, Phys. Rev B **40** (1989) 6175.
7) R. Matz and H. Lüth, Phys. Rev. Lett. **46** (1981) 500.
8) Z. J. Gray-Grychowski, R. G. Egdell, B. A. Joyce, R. A. Stradling and K. Woodbridge, Surf. Sci. **186** (1987) 482.
9) M. G. Betti, U. del Pennino and C. Mariani, Phys. Rev. B **39** (1989) 5887.
10) Y. Chen, S. Nannarone, J. Schaefer, J. C. Hermanson and G. J. Lapeyre, Phys. Rev. B **39** (1989) 7653.
11) U. del Pennino, C. Mariani, A. Amoddeo, R. Biagi, F. Proix and C. Sébenne, J. Phys. Condensed Matter **5** (1993) 6613.
12) A. Ritz and H. Lüth, J. Vacuum Sci. Technol. B **3** (1985) 1153.
13) T. S. Jones, M. Q. Ding, N. V. Richardson and C. F. McConville, Surf. Sci. **247** (1991) 1.
14) Y. Chen, J. C. Hermanson and G. J. Lapeyre, Phys. Rev. B **39** (1989) 12682.
15) R. G. Egdell, S. D. Evans, R. A. Stradling, Y. B. Li, S. D. Parker and R. H. Williams, Surf. Sci. **262** (1992) 444.
16) T. Inaoka and T. Chihara, Surf. Sci. **208** (1989) 71.
17) A. Stahl, Surf. Sci. **134** (1983) 297.
18) T. Inaoka, Surf. Sci. **198** (1988) 491.
19) T. Inaoka, Surf. Sci. **257** (1991) 237.
20) D. H. Ehlers and D. L. Mills, Phys. Rev. B **36** (1987) 1051; B **37** (1988) 1019.
21) S. R. Streight and D. L. Mills, Phy. Rev. B **40** (1989) 10488.
22) H. Yu and J. C. Hermanson, Phys. Rev. B **40** (1989) 11851.
23) see, e.g., H. Ibach and D. L. Mills, Electron Energy Loss Spectroscopy and Surface Vibrations (Academic Press, London, 1982) appendix A.
24) T. Inaoka, to be published in Surf. Sci.
25) E. O. Kane, J. Phys. Chem. Solids **1** (1957) 249.
26) M. Hass and B. W. Henvis, J. Phys. Chem. Solids **23** (1962) 1099.
27) T. Inaoka, D. M. Newns and R. G. Egdell, Surf. Sci. **186** (1987) 290.
28) R. H. Ritchie and A. L. Marusak, Surf. Sci. **4** (1966) 234.